The Astrophysical Journal, 991:97 (7pp), 2025 September 20 https://doi.org/10.3847/1538-4357/ae017f

Measurements of the Perpendicular Correlation Length of Coronal Alfvénic Waves with DKIST

Michael Hahn, Stefan J. Hofmeister, Alexandros Koukras, and Daniel Wolf Savin
Columbia Astrophysics Laboratory, Columbia University, 550 West 120th Street, New York, NY 10027, USA; mhahn@astro.columbia.edu
Received 2025 July 7; revised 2025 August 18; accepted 2025 August 28; published 2025 September 18

Abstract

We have measured the perpendicular correlation length $L_\perp$ of Alfvénic waves in the corona using data from the Daniel K. Inouye Solar Telescope (DKIST) Cryogenic Near Infrared Spectropolarimeter (Cryo-NIRSP) instrument. These data have high spatial resolution and were collected using a raster, enabling us to unambiguously identify the parallel and perpendicular directions with respect to the wave propagation. We find that the measured median $L_\perp \approx 3.5$ Mm, which is about half the value found by previous measurements. We ascribe the smaller value measured here to the improved spatial resolution of DKIST. There is a gradual decrease of $L_\perp$ as a function of frequency. We also computed the spatial correlation length of the observed static density structures and found that their typical correlation lengths of ≈8.4 Mm were significantly larger than those of the waves.

Unified Astronomy Thesaurus concepts: Quiet Sun (1322); Alfvén waves (23); Solar coronal heating (1989); Solar coronal waves (1995); Solar coronal streamers (1486)

1. Introduction

Wave-driven models of coronal heating posit that the energy is transported to the corona by Alfvénic waves, which damp in the corona, thereby converting the energy they carry into particle heating. A challenge for wave-driven models is that the Alfvén waves observed in the corona have long periods and long parallel and perpendicular wavelengths that cannot directly heat the plasma. A number of processes have been proposed that can drive the Alfvénic wave energy to shorter length scales and lead to efficient dissipation of the wave energy into coronal heating. The most commonly modeled such process is turbulence, which arises through the nonlinear interaction between counterpropagating Alfvén waves. This nonlinear interaction drives a cascade of wave energy to shorter perpendicular length scales (e.g., G. G. Howes 2024). Another possible process is the parametric decay instability (PDI), in which an outward propagating Alfvén wave couples to an acoustic wave (i.e., a density fluctuation) and also generates a secondary inward propagating Alfvén wave (M. Shoda & T. Yokoyama 2016; V. Réville et al. 2018; M. Shoda et al. 2018, 2019). PDI may result in heating both because the density fluctuations are more readily damped than the Alfvén waves and because the inward-traveling secondary Alfvén wave contributes to the generation of turbulence as it interacts with outward-traveling waves. A third potential process is phase mixing, which occurs when there is a gradient in the Alfvén speed in the direction transverse to the wave propagation (J. Heyvaerts & E. R. Priest 1983; C. Meringollo et al. 2024). Such gradients are present in the corona due to the flux tube organization of the plasma. Alfvén waves travel at different speeds across these transverse gradients, resulting in a corrugation of the wave front and shorter perpendicular length scales.

In all of the above processes the perpendicular wavelength, $\lambda_\perp$, plays a key role, which can be equivalently expressed as the perpendicular wavenumber $k_\perp$. This is because the parallel electric field of the Alfvén wave is proportional to $k_\perp$ (W. Gekelman et al. 1997; K. Stasiewicz et al. 2000). A stronger parallel electric field leads to stronger interactions with plasma particles through both collisional interactions as well as collisionless Landau damping (C. A. Kletzing et al. 2010). In magnetohydrodynamic turbulence models, these stronger interactions are manifested as increased turbulent diffusivities that result in greater turbulent heating rates (e.g., S. R. Cranmer et al. 2007; M. Shoda et al. 2018).

Models of coronal heating incorporate a perpendicular correlation length $L_\perp$ as a parameter to characterize the largest relevant perpendicular wavelength. This length represents the maximum transverse size of the plasma that is perturbed by the Alfvén wave. Physically, this scale is expected to be set by the driver of the Alfvén wave, analogous to the size of the Alfvén wave antenna in a laboratory plasma.

The measurements presented here are distinct from the correlation length as defined in classical turbulence theory, though they are related. In the theory of homogeneous turbulence, the correlation length is defined from a two-point correlation function averaged over a homogeneous region and results in a single scalar value (G. K. Batchelor 1953; W. H. Matthaeus & M. L. Goldstein 1982). Physically, this value may be considered to represent a typical length scale of turbulent eddies. In contrast, our measurements, and much of the previous work to which we compare, compute correlations relative to a fixed spatial location from which we produce a two-dimensional (2D) map of the correlation. From these maps we we derive anisotropic correlation lengths, which allows us to quantify spatial variations in the wave coherence in the inhomogeneous corona. Our correlation length represents the width of the plasma that is perturbed by the wave, which may correspond to the largest turbulent eddy if turbulence is present.

The perpendicular correlation length increases as the waves propagate upward due to the superradial expansion of the magnetic field. It has been hypothesized that the correlation

length scales in the photosphere might range from 0.1 to 1 Mm, depending on the source of the Alfvén waves (M. Shoda et al. 2018). The smaller value of 0.1 Mm corresponds to the length scales of intergranular magnetic patches (T. E. Berger & A. M. Title 2001; A. A. van Ballegooijen et al. 2011). The larger value of 1 Mm corresponds to the characteristic length scale of velocity fluctuations associated with granular motions (V. I. Abramenko et al. 2013). The relevant length scales moving into the corona are larger as $L_\perp$ grows with the expansion of the magnetic field roughly as $1/\sqrt{B}$ (J. V. Hollweg 1986). Hence $L_\perp$ in the corona depends on both what is driving the Alfvén waves, e.g., vortex flows in magnetic patches versus swaying of flux tubes jostled by granular motions, as well as the expansion of the magnetic field with height.

Until recently, there had been a lack of observational constraints for $L_\perp$ in the corona, and estimates used in models spanned several orders of magnitude (e.g., M. Shoda et al. 2018). However, several recent measurements now exist. R. Sharma & R. J. Morton (2023) studied Doppler velocity fluctuations using the Coronal Multichannel Polarimeter (COMP). For each spatial location in the COMP data, they computed the coherence within the surrounding region of the Doppler oscillations at 3 mHz. This results in an island of high coherence, which is elongated in the direction of wave propagation and for which the perpendicular width is a measure of $L_\perp$. R. Sharma & R. J. Morton (2023) estimated this width to be in the range $L_\perp \approx 7.6$–9.3 Mm. M. Hahn et al. (2025) performed a similar analysis of COMP data, except computing the cross correlation rather than focusing on a specific frequency. M. Hahn et al. (2025) found similar results with a median $L_\perp \approx 7$ Mm. However, COMP has rather low spatial resolution, resulting in a pixel scale that prevents measurements of $L_\perp$ below about 4.5 Mm. M. Hahn et al. (2025) showed that the measured statistical distribution of $L_\perp$ values is consistent with what is expected if the actual $L_\perp$ distribution in the corona includes smaller values that could not be spatially resolved.

A couple of measurements have been performed using similar coherence methods, but with one-dimensional (1D) data from a single spectrometer slit pointing. These measurements have the advantage of high spatial resolution along the slit and fast cadence since the slit is not rastered but suffer from the inability to determine the direction of wave propagation and thereby distinguish the parallel and perpendicular directions. The parallel correlation lengths are very long, so the analysis of data with an undetermined orientation with respect to the waves provides only upper bounds for $L_\perp$. E. Tajfirouze et al. (2025) performed such an analysis using data from the Extreme Ultraviolet Imaging Spectrometer on Hinode and found $L_\perp \approx 8$ Mm. R. J. Morton et al. (2025) performed an analysis using a Daniel K. Inouye Solar Telescope (DKIST) Cryogenic Near Infrared Spectropolarimeter (Cryo-NIRSP; A. Fehlmann et al. 2023) observation and estimated $L_\perp \approx 6$–8 Mm.

Finally, others have suggested that the perpendicular length scales of observed solar structures may be a proxy for $L_\perp$. Z. Bailey et al. (2025) studied a high spatial resolution eclipse image and applied a spatial correlation analysis to characterize the perpendicular length scales of stable density structures. That is, they obtained a measure of the distribution of widths of the observed coronal loops. They found length scales of 4–9 Mm in the corona, which is consistent with the COMP measurements of $L_\perp$. Additionally, they observed that these lengths do increase with height, which represents a direct measurement of the expansion of the magnetic flux tubes. However, it is not clear whether the perpendicular length scale of density structures is the same as the $L_\perp$ for the Alfvénic waves.

Here, we measure $L_\perp$ in the corona using a two-dimensional (2D) raster obtained with DKIST Cryo-NIRSP. The advantages of this observation over previous ones is that the spatial resolution is a factor of 2 better than the COMP measurements, and the 2D raster allows us to unambiguously determine the direction of wave propagation so that we can measure $L_\perp$ rather than a mix of $L_\perp$ and the parallel correlation length, $L_\parallel$. Our measured $L_\perp$ is about half of what was found in previous studies with COMP (R. Sharma & R. J. Morton 2023; M. Hahn et al. 2025), demonstrating that $L_\perp$ was not fully resolved by those studies. Even here, though, there are suggestions that $L_\perp$ may not yet be fully resolved, and higher-resolution measurements should be performed. We also discuss other properties of $L_\perp$ and its frequency dependence, spatial variation, and relationship to the sizes of coronal structures.

The rest of this work is organized as follows: Section 2 describes the DKIST Cryo-NIRSP observation and Section 3 reviews the analysis to determine $L_\perp$. Section 4 presents and discusses the results including maps of $L_\perp$ in the observed region, the dependence of $L_\perp$ on frequency, and the relation between $L_\perp$ and the sizes of observed density structures. Section 5 concludes.

2. Observations

We studied two observations carried out by the DKIST using the Cryo-NIRSP instrument on 2024 June 19 and measuring spectra from the Fe XIII 1074 nm line. The data set IDs in the DKIST database are BJJGP and BLLKX. Both observations had the Cryo-NIRSP spectrometer slit oriented roughly radially with respect to the solar limb. Each observation consisted of a raster scan with 25 steps in the direction perpendicular to the slit with a spacing of about $2\farcs3$ (1.7 Mm) between raster positions. For comparison, the pixel scale along the slit is about $0\farcs12$ (0.09 Mm).

The target for the observations was a quiescent area composed of long nearly radial magnetic fields. The approximate locations are illustrated in Figure 1 superimposed on an image from the Atmospheric Imaging Assembly (AIA; J. R. Lemen et al. 2012) in the 193 Å bandpass. We note that the DKIST pointing in Figure 1 is approximate, as we have not performed a detailed coalignment with AIA. Based on a visual inspection of the morphology, it appears that the nominal DKIST pointing may differ from the AIA coordinates by about $20''$. The absolute pointing, though, is not relevant to our analysis. BJJGP is the observation closer to the solar limb, extending from about 0.97 to 1.21 $R_\odot$. BLLKX is pointed further out, extending from about 1.15 to 1.39 $R_\odot$.

The Cryo-NIRSP exposure time at each position is about 0.725 s, and it takes about 0.2 s to move the slit, resulting in a time step of 0.95 s for each step within a raster. As there are 25 positions within each raster, the total time between each raster is about 25.6 s, which includes additional overhead to reposition to the start of the raster. The lower pointing contained 252 raster scans, though the quality of the data for some of the later raster scans declined, likely due to seeing. So, we conservatively limit our analysis to only the first

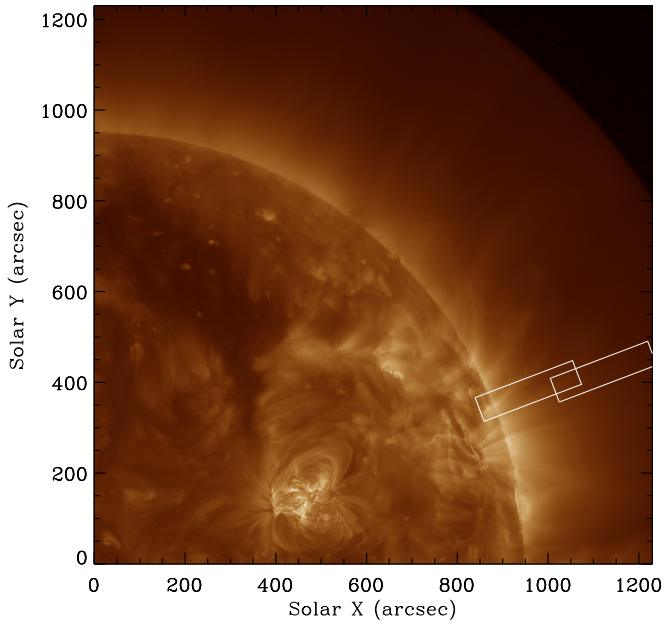

Figure 1. Approximate locations of DKIST observations superimposed on a contemporaneous AIA 193 Å image.

215 rasters or about 1.8 hr of data. The upper pointing contained 125 raster scans (0.9 hr), all of which appeared to be of sufficient quality.

3. Analysis

We fit a Gaussian profile to the observed spectra in order to extract the line centroid, intensity, and width. This fitting was performed using the procedures described by T. A. Schad et al. (2023a, 2023b), which incorporate spectral atlases to account for scattered photospheric and telluric lines in the spectrum.

Our primary interest is the Doppler velocity fluctuations. To obtain a suitable velocity fluctuation time series at each pixel, we first convert the centroid to velocity units. Each raster was collected over about 25.6 s with ∼1 s intervals between the slit pointings that make up the columns of the 2D observation. We adjusted these rastered data by linearly interpolating the Doppler velocity within each raster scan to a common time. Later testing showed, though, that this has little effect on the analysis since the wave periods of interest are several minutes and so significantly longer than the raster cadence. Finally, we subtract the mean velocity in each pixel, thereby obtaining relative Doppler velocity fluctuations, $\delta v(t)$.

The above procedure results in a map of velocity fluctuations $\delta v(t, x, y)$, where x and y refer to the directions perpendicular and parallel to the Cryo-NIRSP slit. These directions are not necessarily aligned with the waves. So, in order to determine the perpendicular correlation length, $L_\perp$, we first must determine the direction of wave propagation, which defines the parallel and perpendicular directions with respect to the waves. We used two methods to do this, which are very similar.

First, we used a cross-correlation method (S. Tomczyk et al. 2007; M. Hahn et al. 2025). That is, for each pixel, we computed the cross correlation c between $\delta v(t)$ at that pixel and at all of its neighbors within a region of about $\pm 27''$. This size was sufficient to accurately capture the high-correlation region. The cross-correlation calculation reveals an island of high cross correlation that is elongated along the direction of wave travel. We identified the set of pixels with a high correlation, $c > 0.6$, which was chosen by inspection as providing a good balance between having sufficient data points to identify the orientation with good precision and also providing a reasonable noise cutoff. In order to identify the perpendicular and parallel directions at the reference pixel, we characterize the orientation of the island by finding the slope of the line that would minimize the sum of the perpendicular distances between the high-correlation points and the line. This fitting was performed using a principal component analysis (see M. Hahn et al. 2025).

We also performed the analysis in a frequency-resolved way using a coherence analysis. Like the cross-correlation method, we selected a reference pixel and then computed the coherency spectrum with all of its neighbors within $\pm 27''$. The coherency spectrum, $k(f)$ is given by

$$k_{ij}(f) = \frac{|P_{ii}(f)|^2}{P_{ij}(f)P_{jj}(f)}, \quad (1)$$

where P_{ij} is the Fourier cross spectrum between the time series $\delta v(t)$ at pixel i and that at pixel j and P_{ii} or P_{jj} are the Fourier power spectra (G. M. Jenkins & D. G. Watts 1968). A subtlety of the coherence calculation is that the Fourier spectra must be averaged in some way, as $k(f)$ for a single time series is always unity. This averaging is performed by breaking the full time series into segments, computing the Fourier spectra for each segment, averaging those Fourier spectra, and then computing the coherence. A tradeoff is that each segment contains fewer data points than the whole time series, thereby reducing the frequency resolution. Here, we have used $N = 8$ segments overlapping by 50%. This appeared to give a converged estimate of $k(f)$, while maintaining a reasonable frequency resolution of $\Delta f = 1.3$ mHz for the lower pointing and $\Delta f = 2.3$ mHz for the upper pointing. Once the coherence map $k(f)$ for a given reference pixel has been computed, we measured the orientation of the island of high k for each frequency using the same analysis as for the cross-correlation method.

For both the cross-correlation or coherence methods, we derive $L_\perp$ using the method of M. Hahn et al. (2025). The island of high coherence is maximum at the reference pixel and declines away from it roughly as a Gaussian. To determine $L_\perp$ we integrate the coherence along the parallel direction and then fit the resulting curve $k(x;f)$ with a Gaussian, where x represents the coordinate in the direction perpendicular to the wave propagation. Following the convention that these lengths are usually reported as exponential lengths rather than Gaussian widths, we multiply the Gaussian width by $\sqrt{2}$ to obtain $L_\perp$ (R. Sharma & R. J. Morton 2023).

4. Results and Discussion

We have produced maps of $L_\perp$ for various frequencies in both the lower and upper fields of view. Figure 2 shows an example of $L_\perp$ derived from the coherence analysis for the lower pointing at a frequency of $f = 3.9$ mHz. The two black curves in the figure illustrate two example trajectories of Alfvénic waves through the field of view. These trajectories were obtained by stepping along the wave path according to the parallel wave direction inferred during the coherence

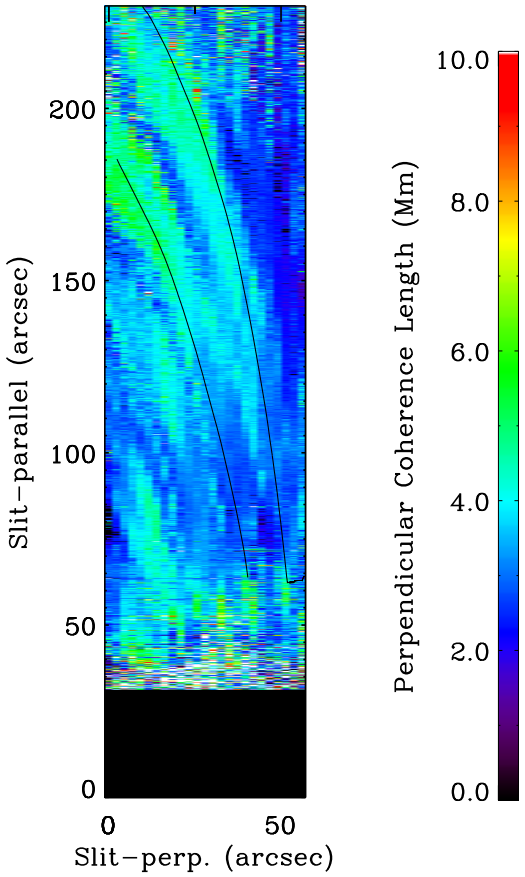

Figure 2. Map of $L_\perp$ in the lower pointing observation using the coherence method at 3.9 mHz. The black curves superimposed on the image illustrate two examples of the paths of Alfvénic waves obtained by stepping along the parallel direction inferred at each pixel. The bottom of the observation is masked due to overlapping with the solar limb.

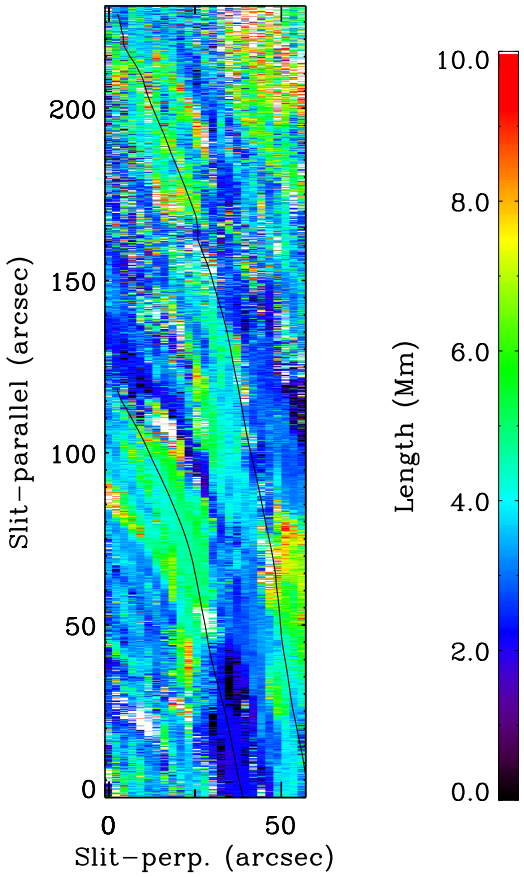

Figure 3. Same as Figure 2 but for the upper pointing using the coherence method at 2.3 mHz.

analysis (see M. Hahn et al. 2025). These trajectories are expected to follow the magnetic field and therefore represent two of the many field lines threading through the image. Figure 3 is a similar map, plotting $L_\perp$ at $f = 2.3$ mHz for the upper pointing. These selected frequencies are near a peak in the Alfvénic wave power spectrum and so have a good signal-to-noise ratio. The maps of $L_\perp$ at other frequencies are qualitatively similar, though with more scatter. The frequency dependence of $L_\perp$ is discussed in more detail in Section 4.1.

One feature of these maps is that $L_\perp$ clearly shows structure, exhibiting ridges of high $L_\perp$ that follow the wave trajectories. The Alfvénic waves travel along the magnetic field. So, it appears that $L_\perp$ varies among coronal loops or flux tubes. The relatively high spatial resolution of DKIST is what allows us to see this structure. Previous lower resolution measurements with COMP showed that the corona appeared roughly homogeneous in $L_\perp$ (R. Sharma & R. J. Morton 2023) or showed significant differences mainly between broad classes of structure such as short loops versus long streamers (M. Hahn et al. 2025).

A more subtle feature of the maps is that there appears to be an increase of $L_\perp$ along the path of the waves. This is especially visible in the lower pointing, where $L_\perp$ increases from roughly 3 Mm at the base of the corona up to about 5 Mm near the top of the slit. However, this increase appears limited to the ridges of high $L_\perp$, and we do not see a general increase of $L_\perp$ with height. The trend is not as clear in the upper pointing, possibly due to the impact of noise at these larger heights. The increase of $L_\perp$ with height is physically expected as the waves propagate within the expanding magnetic flux tubes.

Overall, the typical value of $L_\perp$ in these observations is in the range of 3–5 Mm, which is significantly smaller than those found in previous measurements using COMP (R. Sharma & R. J. Morton 2023; M. Hahn et al. 2025) or single-slit sit-and-stare observations (R. J. Morton et al. 2025; E. Tajfirouze et al. 2025). R. Sharma & R. J. Morton (2023) estimated $L_\perp$ to be in the range of about 7.6–9.3 Mm, and M. Hahn et al. (2025) found the median $L_\perp$ to be 7 Mm. So, the values we find here are about half of what was found in the earlier measurements. It is notable that 2.″3 raster pointing of DKIST is about half the 4.″5 pixel scale of COMP, which is consistent with spatial resolution being a limiting factor in previous measurements.

4.1. Frequency Dependence

Figure 4 presents the histograms of the $L_\perp$ measurements from the lower pointing. The results from the upper pointing are very similar. The histograms show that the distribution of $L_\perp$ values resembles a log-normal distribution, as has been seen previously (R. Sharma & R. J. Morton 2023; M. Hahn et al. 2025). The distribution of correlation lengths measured in the solar wind has been found to be log-normal (M. E. Ruiz et al. 2014), so the distribution found here may indicate that this distribution starts in the low corona. Alternatively, M. Hahn et al. (2025) have shown that systematic effects,

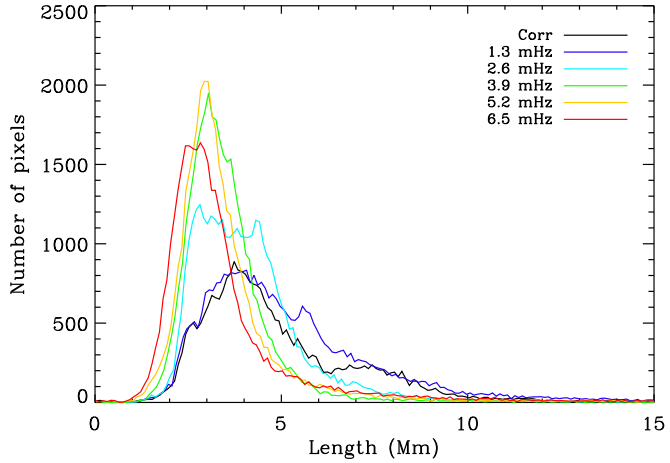

Figure 4. Histograms of the $L_\perp$ values obtained among all the above-limb pixels in the lower pointing observation. The black curve corresponds to the results obtained using the cross correlation, and the different colors are for the indicated frequencies of the coherence method.

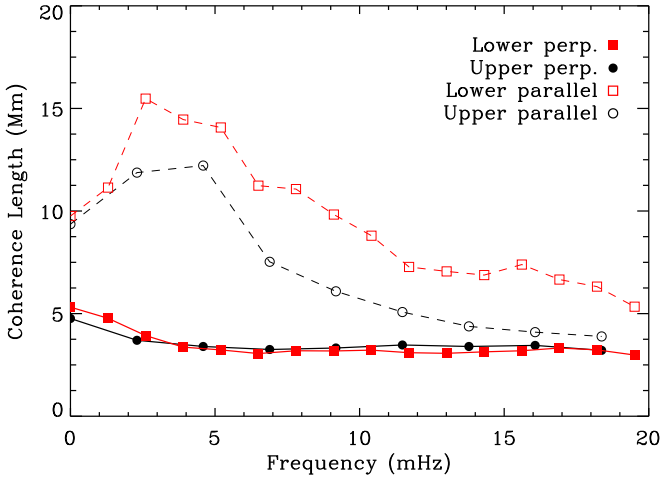

Figure 5. Median $L_\perp$ (solid symbols) and $L_\parallel$ (open symbols) from the coherence method as a function of frequency for the lower (red squares) and upper pointings (black circles).

such as spatial resolution and line-of-sight integration, could distort a power-law distribution in such a way that it resembles a log-normal one. So, the physical interpretation of these distributions is not yet clear.

The measurement using correlation most closely resembles the lowest-frequency coherence measurements. This is likely because the power in the δv fluctuations declines as a power law with increasing frequency, and so, since the correlation measurement implicitly averages over frequency, it is dominated by the lowest-frequency fluctuations that have the most power. The peak of the distribution is below 5 Mm for every frequency, but there is a long tail toward higher values. There are almost no measurements of $L_\perp$ below 1 Mm, which may be a limit set by the spatial resolution. M. Hahn et al. (2025) suggested that the log-normal form of the $L_\perp$ distribution was consistent with an unresolved population of small $L_\perp$ values, and that may be true for this observation as well. However, we also see that the falloff in the distribution on the short side of the peak is more gradual than the abrupt falloff seen in M. Hahn et al. (2025), which might indicate that we now do marginally resolve the smallest relevant $L_\perp$ values, and there actually are not many places where $L_\perp$ is below 1 Mm.

There is a tendency for $L_\perp$ to decrease with increasing frequency, as can be seen in Figure 4. In order to show this trend more clearly, Figure 5 plots the median $L_\perp$ at each frequency of the coherence measurements for both the lower and upper pointing. The median $L_\perp$ is largest at the lowest frequency but decreases to a roughly constant value at higher frequencies. This trend is gradual, and one can see from Figure 4 that the systematic shift with frequency is smaller than the spread of $L_\perp$ at a given frequency. A decrease of $L_\perp$ with frequency has also been noted by R. J. Morton et al. (2025), who interpreted this as a potential signature of turbulent phenomena, such as dynamic alignment (S. Boldyrev 2006), although turbulence theory predicted steeper slopes than what R. J. Morton et al. (2025) found. The observed decrease here is much less steep than that found by R. J. Morton et al (2025). For example, in their measurements $L_\perp$ declines from about 9 Mm at 2 mHz to about 4 Mm at 10 mHz, a factor of about 2, whereas our results show a decrease of only ∼20% in that frequency range.

It is not clear why our measurements of $L_\perp(f)$ fall off much more slowly than those of R. J. Morton et al. (2025), but one possibility is that the fall off is due to uncertainty in the identification of the parallel and perpendicular directions combined with bias from the parallel correlation length, $L_\parallel$. The region of high coherence from which we derive $L_\perp$ is approximately a 2D Gaussian. A cross section of this Gaussian is an ellipse whose minor and major axes have lengths $L_\perp$ and $L_\parallel$, respectively. If the inferred orientation of the wave trajectory differs from the true trajectory by an angle θ, then measured perpendicular correlation length $L_{\rm meas}$ is a mix of $L_\parallel$ and $L_\perp$:

$$L_{\rm meas} = \sqrt{L_\perp^2 \cos^2(\theta) + L_\parallel^2 \sin^2(\theta)}. \quad (2)$$

Building on this, we can potentially explain the differences between the results of R. J. Morton et al. (2025) and our own.

We find that there is a strong decrease of $L_\parallel$ with frequency. As shown in Figure 5, at low frequencies below 5 mHz we find $L_\parallel \approx$ 10–15 Mm, which decreases to about 4–5 Mm at $f = 20$ mHz. The interpretation of $L_\parallel$ is complex. In principle, $L_\parallel$ for a propagating wave is infinite, but in practice it may be limited by inhomogeneities in the plasma that cause phase decorrelations with distance such as phase mixing or turbulence and by measurement noise.

These factors may explain the strong observed frequency dependence. For example, if the dominant limiting factor is measurement noise, then $L_\parallel$ may be proportional to the signal-to-noise ratio. It has been shown previously that the power spectrum of Alfvénic fluctuations in the corona declines as a power law with frequency (S. Tomczyk & S. W. McIntosh 2009; M. Hahn et al. 2025; R. J. Morton et al. 2025), which also appears to be true for the present data. Assuming a constant noise level (white noise), the signal-to-noise ratio would follow the same power law, leading to $L_\parallel \propto f^{-\alpha}$, where $\alpha \approx 1.6$ (R. J. Morton et al. 2025). Regardless of the mechanism, given the large value of $L_\parallel$ and its rapid decline with frequency, even a small θ can produce a significant decline in $L_{\rm meas}$ as a function of frequency. The strong decrease in of $L_\perp$ with f seen by R. J. Morton et al. (2025) may be due to not orienting the spectrometer slit perpendicular to the wave trajectories. There may be additional real decreases

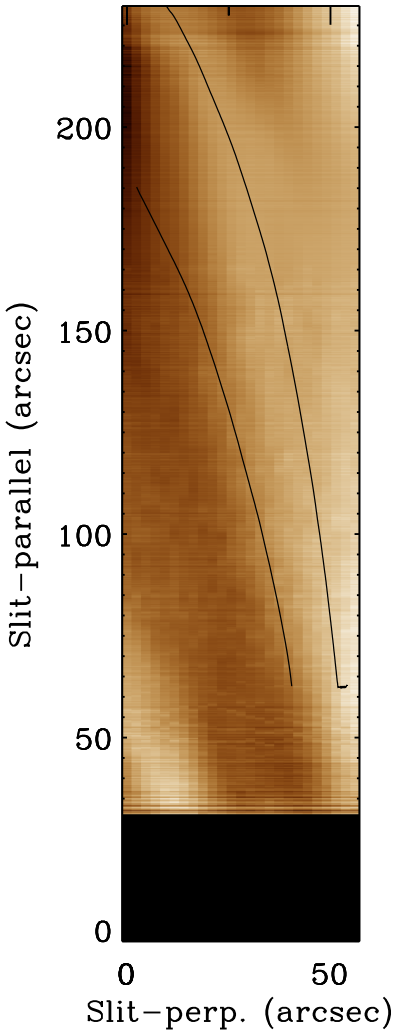

Figure 6. Image in the Fe XIII 1074 nm line observed by DKIST Cryo-NIRSP within the lower pointing field of view. The structure has been enhanced by applying a radial filter, and the intensity units are arbitrary. The black curves illustrate the same sample wave trajectories as shown in Figure 2.

of $L_\perp(f)$, but distinguishing them from this systematic effect requires an accurate assessment of the wave trajectory.

4.2. Relation to Widths of Density Structures

Z. Bailey et al. (2025) have suggested that the widths of static density structures, $S_\perp$, may be a proxy for $L_\perp$. They quantified these widths by studying a high-resolution eclipse image of the corona that had been processed to remove the radial density gradient. They selected the intensity along various 1D cuts across the density structures tracing out coronal magnetic field lines. For each cut, they computed the spatial autocorrelation for different spatial lags along the cut. The correlation length $S_\perp$ was determined by fitting an exponential to the autocorrelation as a function of the lag distance.

We have performed a similar analysis using the intensity data from DKIST. Figure 6 shows the intensity of the Fe XIII 1074 nm line for the lower pointing field of view. The radial density gradient has been removed using the method of H. Morgan et al. (2006). That is, we first found the average, $\bar{I}(r)$, and standard deviation, $\sigma_I(r)$, of the intensity among all pixels at a given radius. Then, the radially filtered intensity is

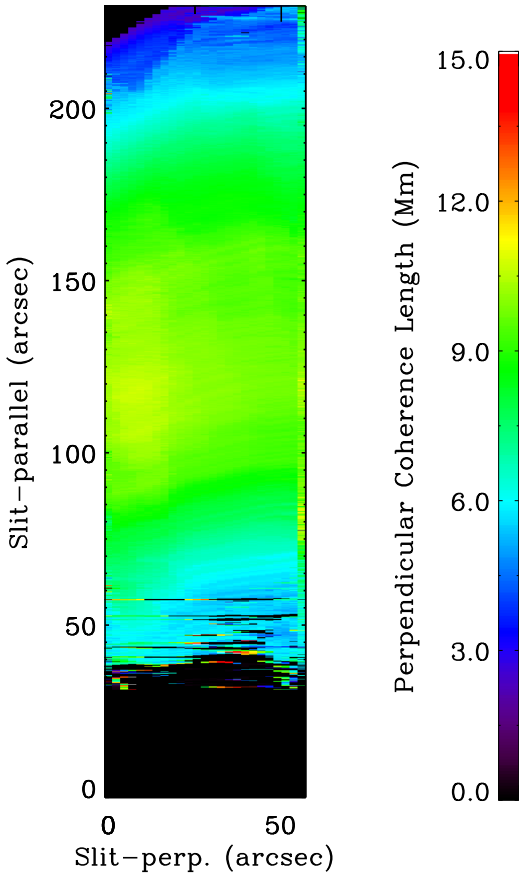

Figure 7. Perpendicular correlation length of the radially filtered intensity from Figure 6. Here the perpendicular direction is the defined from the coherence analysis at 3.9 mHz.

obtained by subtracting the averaged intensity corresponding to each pixel's position and dividing by the standard deviation.

We measured $S_\perp$ from Figure 6. For each pixel we know the direction of wave propagation from the coherence analysis. Specifically, we took the direction from the 3.9 mHz coherence measurement. The results, though, are not sensitive to this choice as the wave propagation direction is determined by the orientation of the magnetic field, and we confirmed that the various frequencies yield similar results. We then selected the intensities $I(s)$ along the perpendicular cut through each pixel and computed the spatial autocorrelation $a(l)$ as a function of spatial lag l:

$$a(l) = \frac{1}{N}\sum_{s=1}^{N-l}(I(s) - \bar{I})(I(s+l) - \bar{I}). \quad (3)$$

Here, $\bar{I}$ is the average intensity along the cut. We estimated $S_\perp$ as the distance at which the autocorrelation falls to $1/e$ of its value at zero lag. The resulting map of $S_\perp$ is shown in Figure 7.

The median $S_\perp$ found in this observation is about 8.4 Mm, which is more than twice as large as the median $L_\perp$. $S_\perp$ within this observation appears to be small at low heights, grow somewhat, and then decline again at larger heights. However, this dependence may be biased by the limited field of view. Figure 6 suggests that the overall density structures are broadest near the center of this image, but that is partly because of the angle at which the magnetic field lines pass through the field of view. There may also be systematic effects due to truncation of

the cuts over which the autocorrelation is calculated, which are shorter near the top and bottom of the field of view since the perpendicular direction is tilted with respect to the slit orientation. Also, the relatively narrow field of view may bias the measurement as there are few distinct structures that fall within the observation. Despite these potential limitations, we find no correlation between the $S_\perp$ derived from the density structure of the corona (Figure 7) and the $L_\perp$ derived from the coherence of the δv fluctuations (Figure 2).

5. Conclusions

We find that the typical $L_\perp$ in the corona is about 3.5 Mm, which is about half of what has been found in other recent studies. The smaller value found here is most likely due to the improved spatial resolution in these DKIST Cryo-NIRSP measurements. Even higher spatial resolution may be needed to definitely resolve $L_\perp$ in the corona.

There are significant spatial variations of $L_\perp$ within the corona. Ridges and troughs of high and low $L_\perp$ appear to follow the magnetic field lines and are aligned with the wave trajectories. $L_\perp$ appears to increase slightly with increasing distance from the Sun along the magnetic field, which is probably proportional to the magnetic expansion of the loop.

We found that the measured $L_\perp$ decreased with increasing frequency, although the decrease we found was much more gradual than the stronger decrease found by R. J. Morton et al. (2025). There are several systematic uncertainties that might account for this, including that the strong decrease may have been due primarily to variation in the parallel coherence length rather than to $L_\perp$.

We did not find any relation between the $L_\perp$ associated with Alfvénic waves and the $S_\perp$ associated with the widths of coronal density structures. The magnitudes of these correlation lengths differ by a factor of a few, and their spatial variations bear no resemblance to one another. However, it is possible that our results represent a somewhat biased view, since the Cryo-NIRSP field of view is narrow and there are only a few evident structures visible.

Acknowledgments

We acknowledge support from NSF AST Grant AST-2005887 and NSF SHINE Grant AGS-2229100.

Software: IDL, solarsoft (S. L. Freeland & B. N. Handy 1998, 2012).

Facility: DKIST.

ORCID iDs

Michael Hahn https://orcid.org/0000-0001-7748-4179
Stefan J. Hofmeister https://orcid.org/0000-0001-7662-1960
Alexandros Koukras https://orcid.org/0000-0002-6232-5527
Daniel Wolf Savin https://orcid.org/0000-0002-1111-6610

References

Abramenko, V. I., Zank, G. P., Dosch, A., et al. 2013, ApJ, 773, 167
Bailey, Z., Bandyopadhyay, R., Habbal, S., & Druckmüller, M. 2025, ApJL, 980, 20
Batchelor, G. K. 1953, The Theory of Homogeneous Turbulence (New York: Cambridge Univ. Press)
Berger, T. E., & Title, A. M. 2001, ApJ, 553, 449
Boldyrev, S. 2006, PhRvL, 96, 115002
Cranmer, S. R., van Ballegooijen, A. A., & Edgar, R. J. 2007, ApJS, 171, 520
Fehlmann, A., Kuhn, J. R., Schad, T. A., et al. 2023, SoPh, 298, 5
Freeland, S. L., & Handy, B. N. 1998, SoPh, 182, 497
Freeland, S. L., & Handy, B. N., 2012 SolarSoft: Programming and Data Analysis Environment for Solar Physics, Astrophysics Source Code Library, ascl:1208.013
Gekelman, W., Vincena, S., Leneman, D., & Maggs, J. 1997, JGR, 102, 7225
Hahn, M., Fu, X., Hofmeister, S. J., et al. 2025, ApJ, 984, 69
Heyvaerts, J., & Priest, E. R. 1983, A&A, 117, 220
Hollweg, J. V. 1986, JGR, 91, 4111
Howes, G. G. 2024, JPlPh, 90, 905900504
Jenkins, G. M., & Watts, D. G. 1968, Spectral Analysis and its Applications (San Francisco: Holden-Day)
Kletzing, C. A., Theucks, D. J., Skiff, F., Bounds, S. R., & Vincena, S. 2010, PRL, 104, 095001
Lemen, J. R., Title, A. M., Akin, D. J., et al. 2012, SoPh, 275, 17
Matthaeus, W. H., & Goldstein, M. L. 1982, JGR, 87, 6011
Meringollo, C., Pucci, F., Nisticó, G., et al. 2024, A&A, 688, 12
Morgan, H., Habbal, S. R., & Woo, R. 2006, SoPh, 236, 263
Morton, R. J., Molnar, M., Cranmer, S. R., & Schad, T. A. 2025, ApJ, 982, 104
Réville, V., Tenerani, A., & Velli, M. 2018, ApJ, 866, 38
Ruiz, M. E., Dasso, S., Matthaeus, W. H., & Weygand, J. M. 2014, SoPh, 289, 3917
Schad, T. A., Fehlmann, A., Dima, G. I., et al. 2023b, ApJ, 965, 40
Schad, T. A., Kuhn, J. R., Fehlmann, A., et al. 2023a, ApJ, 948, 59
Sharma, R., & Morton, R. J. 2023, NatAs, 7, 1301
Shoda, M., Suzuki, T. K., Asgari-Targhi, M., & Yokoyama, T. 2019, ApJ, 880, L2
Shoda, M., & Yokoyama, T. 2016, ApJ, 820, 123
Shoda, M., Yokoyama, T., & Suzuki, T. K. 2018, ApJ, 853, 190
Stasiewicz, K., Bellan, P., Chaston, C., et al. 2000, SSRv, 92, 853
Tajfirouze, E., Morton, R., & Young, P. R. 2025, ApJ, 982, 59
Tomczyk, S., & McIntosh, S. W. 2009, ApJ, 697, 1384
Tomczyk, S., McIntosh, S. W., Keil, S. L., et al. 2007, Sci, 317, 1192
van Ballegooijen, A. A., Asgari-Targhi, M., Cranmer, S. R., & DeLuca, E. E. 2011, ApJ, 736, 3